Supporting Information

Heterointerface regulation of covalent organic framework-anchored graphene *via* a solvent-free strategy for high-performance supercapacitor and hybrid capacitive deionization electrodes

Liming Xu,[a] Yong Liu,[b*] Xiaoyang Xuan[c*], Xingtao Xu,[d] Yuquan Li,[e] Ting Lu,[a] Likun Pan [a*]

[a] *Shanghai Key Laboratory of Magnetic Resonance, School of Physics and Electronic Science, East China Normal University, Shanghai 200241, China*

[b] *School of Materials Science and Engineering, Qingdao University of Science and Technology, Qingdao, Shandong 266042, China*

[c] *College of Chemistry and Chemical Engineering, Taishan University, Taian, Shandong 271000, China*

[d] *Marine Science and Technology College, Zhejiang Ocean University, Zhoushan, Zhejiang 316022, China*

[e] *College of Environmental Science and Engineering, Yangzhou University, Yangzhou, Jiangsu 225127, China*

**Corresponding authors*

Email: lkpan@phy.ecnu.edu.cn (Likun Pan); yong.liu@qust.edu.cn (Yong Liu); xyxuan@tsu.edu.cn (Xiaoyang Xuan)

Materials

Benzene-1,2,4,5-tetraamine tetrahydrochloride (BA, 97%) was purchased from Bide Pharmatech Ltd. Hexaketocyclohexane octahydrate (HC, 98%) was purchased from Meryer (Shanghai) Chemical Technology Co., Ltd. P-toluenesulfonic acid monohydrate (PTSA, 98%), polyvinylidene fluoride (PVDF, ≥99.5%), 1-methyl-2-pyrrolidone (NMP, ≥99.5%), and sodium chloride (NaCl, ≥99.5%) purchased from Sinopharm Chemical Reagent Co., Ltd (Shanghai, China). AC (4~7 μm) was purchased from Kuraray (Shanghai) Co., Ltd. All the chemicals were used without further purification.

Structural characterizations

The microstructure of the samples was observed by scanning electron microscopy (SEM, Hitachi S-4800) and field emission transmission electron microscopy (TEM, JEM 2010 JEOL). The crystal structure was examined by X-ray diffraction (XRD, Panalytical PRO PW3040/60) with Cu Kα (λ=1.54056 Å). The chemical structure and elemental composition were observed by Fourier Transform Infrared Spectrometer (FT-IR, Nicolet iS-50) and powder X-ray photoelectron spectroscopy (XPS, Thermo ESCALAB 250XI). Specific surface area and pore size distribution were calculated by the Brunauer-Emmett-Teller (BET, Autosorb iQ) method, and the density functional theory pore model of Barret-Joyner-Halenda was used to analyze the specific surface area and pore size distribution.

Preparation of working electrode

80 wt.% active material, 10 wt.% Super P (conductive agent) and 10 wt.% polyvinylidene fluoride (binder) were mixed in 1-methyl-2-pyrrolidone to form a homogeneous slurry. Then, the slurry was uniformly cast on graphite substrates (4 cm^2 for the three-electrode system and 32 cm^2 for the CDI cell). Finally, the working electrode was dried at 80 ℃ under vacuum conditions overnight. For the electrochemical and desalination tests, the mass loading of active material on the working electrode was about 4 mg and 60 mg, respectively.

Electrochemical characterizations

The electrochemical performance of the working electrode was measured by cyclic voltammetry (CV), galvanostatic charge-discharge (GCD), and electrochemical impedance spectroscopy (EIS) in an open environment using a CHI660E electrochemical analyzer (Shanghai, China) with 1 M NaCl solution as electrolyte. In the three-electrode system, Ag/AgCl and a platinum mesh were used as the reference and counter electrodes, respectively.

Electrochemical calculation

For the three-electrode system, the specific capacitance (C_{S1}, F g^{-1}) of the material was calculated from CV curves according to the following formula:[1]

$$C_{S1} = \frac{\int_{E_1}^{E_2} i(E)d(E)}{2mv(E_2 - E_1)} \quad \text{(S1)}$$

where E_1 and E_2 are the cutoff potentials in CV, i(E) is the instantaneous current, i(E)d(E) is the total voltammetric charge obtained by integration of the positive and negative sweeps in the CV, v is the scan rate, and m is the mass of the individual sample. The specific capacitance (C_{S2}, F g^{-1}) was calculated from the GCD curves according to the following equation:[2]

$$C_{S2} = \frac{I * \Delta t}{m * \Delta V} \quad \text{(S2)}$$

where I, Δt, m, and ΔV, refer to the current (A), discharge time (s), mass of active material (g), and potential window (V), respectively.

For the two-electrode system, the specific capacitance (C_{S3}, F g^{-1}) was calculated by the following formula:[3]

$$C_{S3} = \frac{I * \Delta t}{m * \Delta V} \quad \text{(S3)}$$

where I, ΔV, Δt, and m are the discharge current (A), the voltage window (V), the discharge time (s), and the total mass (g) of the active material of two electrodes, respectively. The energy density (E, Wh kg^{-1}) and power density (P, W kg^{-1}) were calculated by the following two equations:[4]

$$E = \frac{C_{S3} * \Delta V^2}{2 * 3.6} \quad \text{(S4)}$$

$$P = \frac{3600 * E}{\Delta t} \quad \text{(S5)}$$

where C_{S3}, Δt, and ΔV are specific capacitances (F g^{-1}), discharge time (s), and voltage window (V).

Desalination tests

All desalination experiments were carried out in a batch-mode HCDI system with continuously

circulating the NaCl solution through the HCDI unit by using a peristaltic pump (volume: 70 mL, flow rate: 100 mL min^{-1}, temperature: room temperature). The concentration of the pump effluent was recorded in real-time by an ion conductivity meter (DDSJ-308A, Precision & Scientific Instrument). The working electrode of HCDI consists of a BAHC/BAHCGO cathode and an AC anode separated by a spacer and anion/cation-exchange membrane. The desalination experiments of NaCl solutions with different initial concentrations (100, 200, 300, 500, 1000 mg L^{-1}) were carried out at ±1.6 V, while different current densities (50, 100, 150, 200, 250 mA g^{-1}) were employed for the tests in 500 mg L^{-1} NaCl solution. Our previous work described the relationship between NaCl solution conductivity and concentration.[5]

Desalination calculation

The desalination capacity (SAC, mg g^{-1}), mean desalination rate (MSAR, mg g^{-1} min^{-1}), and charge efficiency (Λ) were defined as follows: [6,7]

$$SAC = \frac{(C_0 - C_e) * V}{m} \quad \text{(S6)}$$

$$MSAR = \frac{SAC}{t} \quad \text{(S7)}$$

$$\Lambda = \frac{(C_0 - C_e) * V * F}{1000 * M * Q} * 100\% \quad \text{(S8)}$$

where C_0 and C_e are the initial and final NaCl concentrations (mg L^{-1}), V is the volume of NaCl solution (L), m is the mass of the active materials (g), t (s) is the charge time, F is the Faraday constant (96,485 C mol^{-1}), M (58.44 g mol^{-1}) is the relative molar mass of NaCl, and Q (charge, C) is the total charge.

Complex capacitance calculation

The complex capacitance (C(ω), F) was defined as follows: [6,7]

$$SAC = \frac{(C_0 - C_e) * V}{m} \quad \text{(S6)}$$

$$MSAR = \frac{SAC}{t} \quad \text{(S7)}$$

where C_0 and C_e are the initial and final NaCl concentrations (mg L^{-1}), V is the volume of NaCl solution (L), m is the mass of the active materials (g), t (s) is the charge time, F is the Faraday constant (96,485 C mol^{-1}), M (58.44 g mol^{-1}) is the relative molar mass of NaCl, and Q (charge, C) is the total charge.

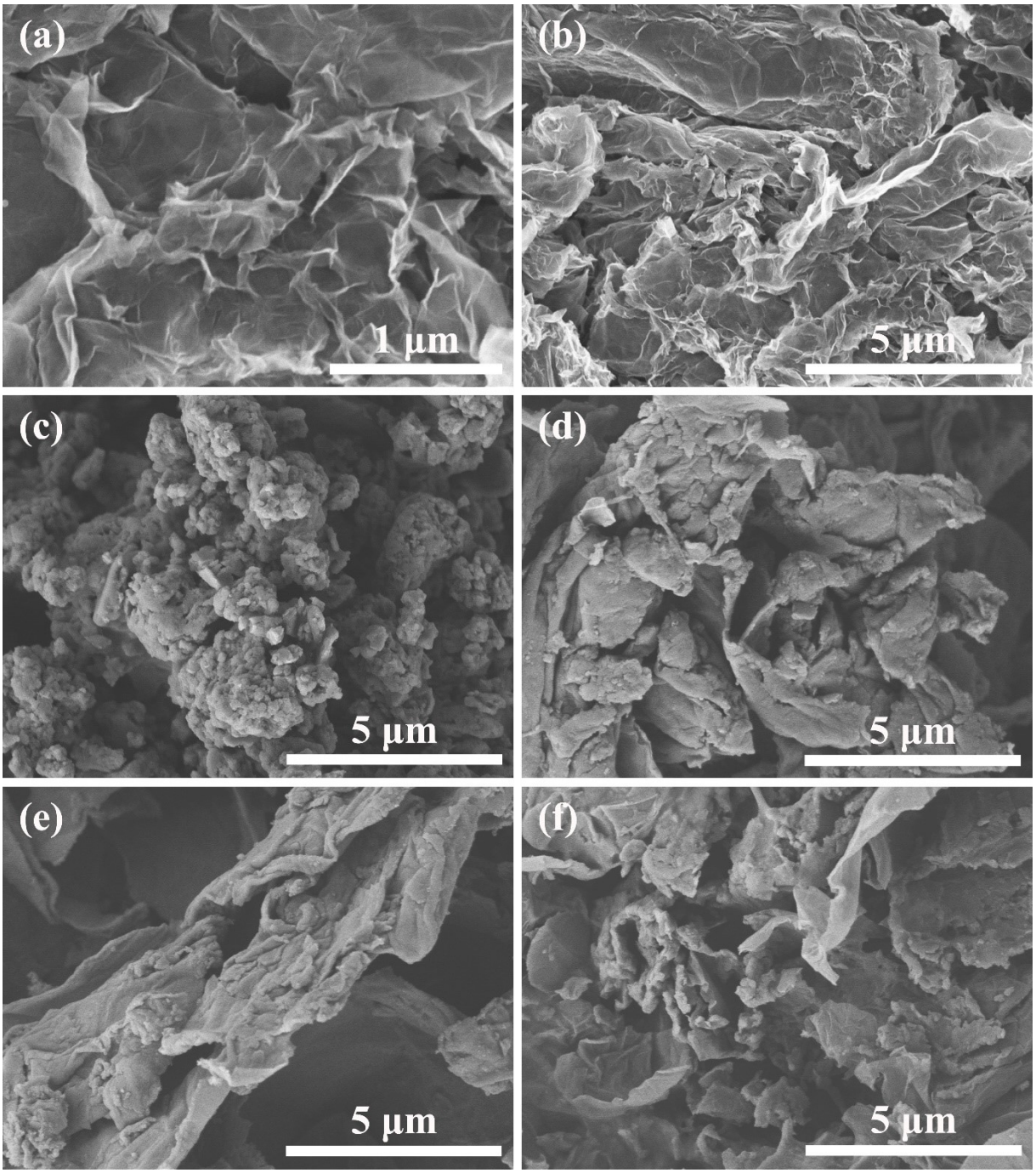

Fig. S1. SEM images of (a,b) rGO, (c) BAHC, (d) BAHCGO-50, (e) BAHCGO-75, and (f) BAHCGO-100.

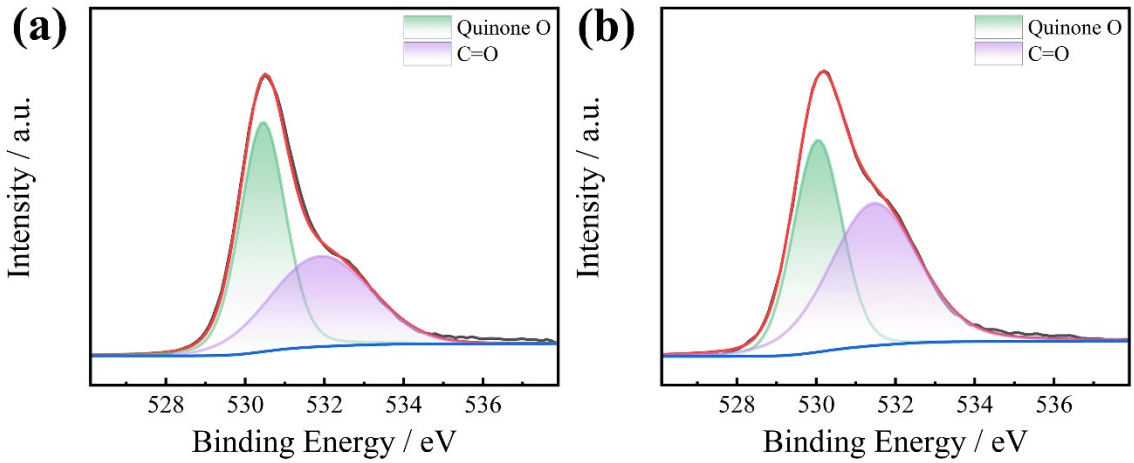

Fig. S2. High-resolution XPS O 1s spectra of (a) BAHC and (b) BAHCGO-75.

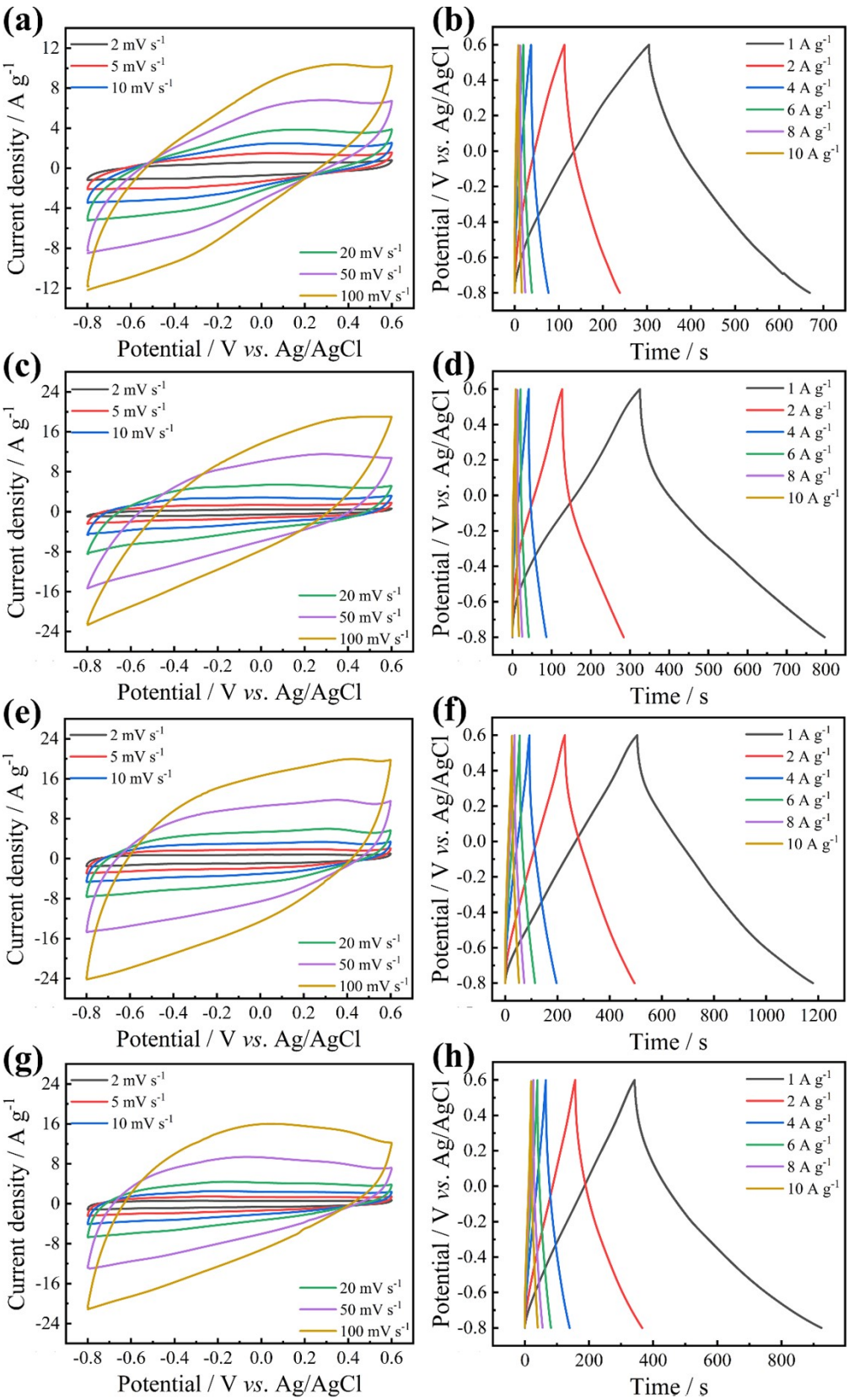

Fig. S3. Electrochemical performances of (a, b) BAHC, (c, d) BAHCGO-50, (e, f) BAHCGO-75, and (g, h) BAHCGO-100 under the three-electrode system.

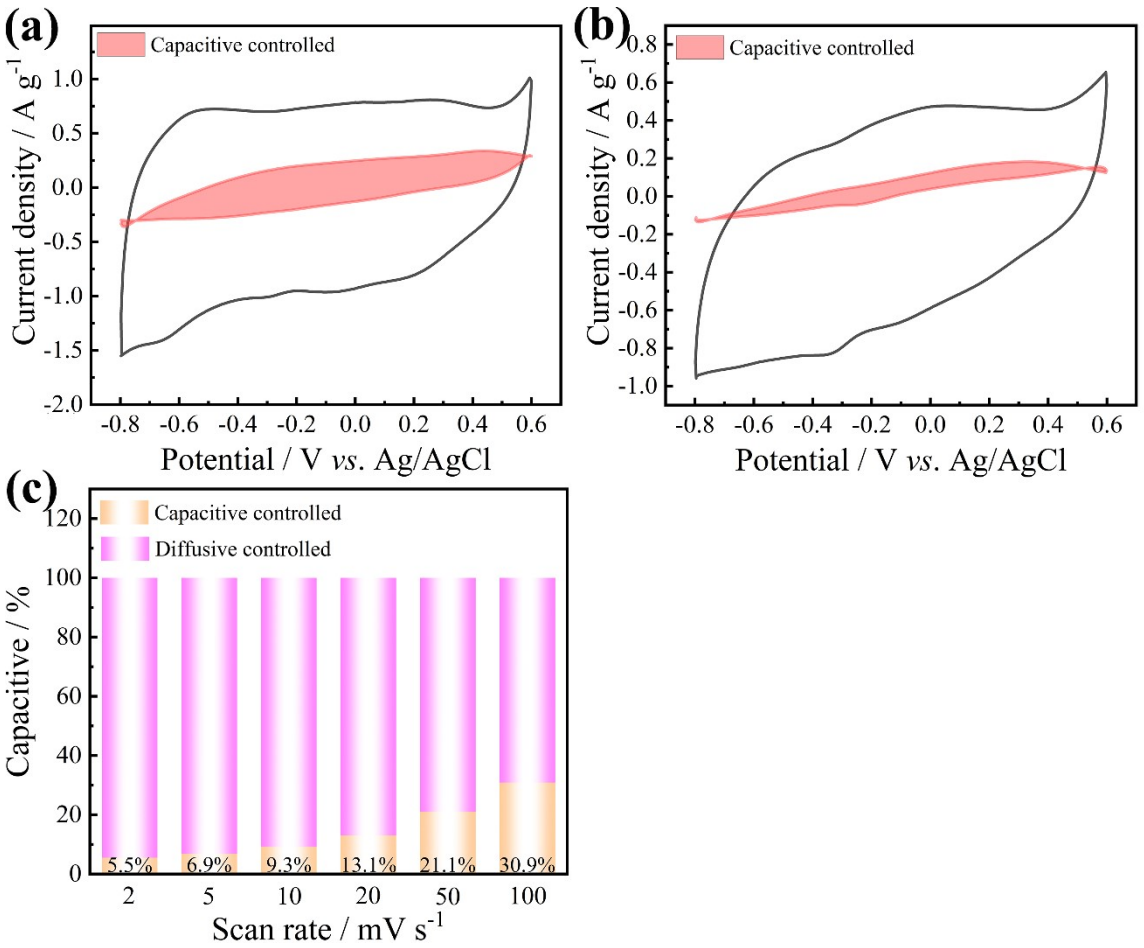

Fig. S4. CV curves with the capacitive contribution of (a) BAHCGO-75 and (b) BAHC at 2 mV s^{-1}. Percentages of capacitive and diffusion contributions of (c) BAHC.

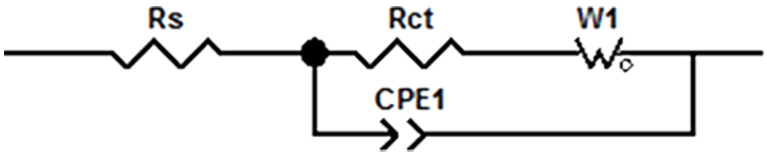

Fig. S5. The fitting equivalent circuit diagram of the EIS test.

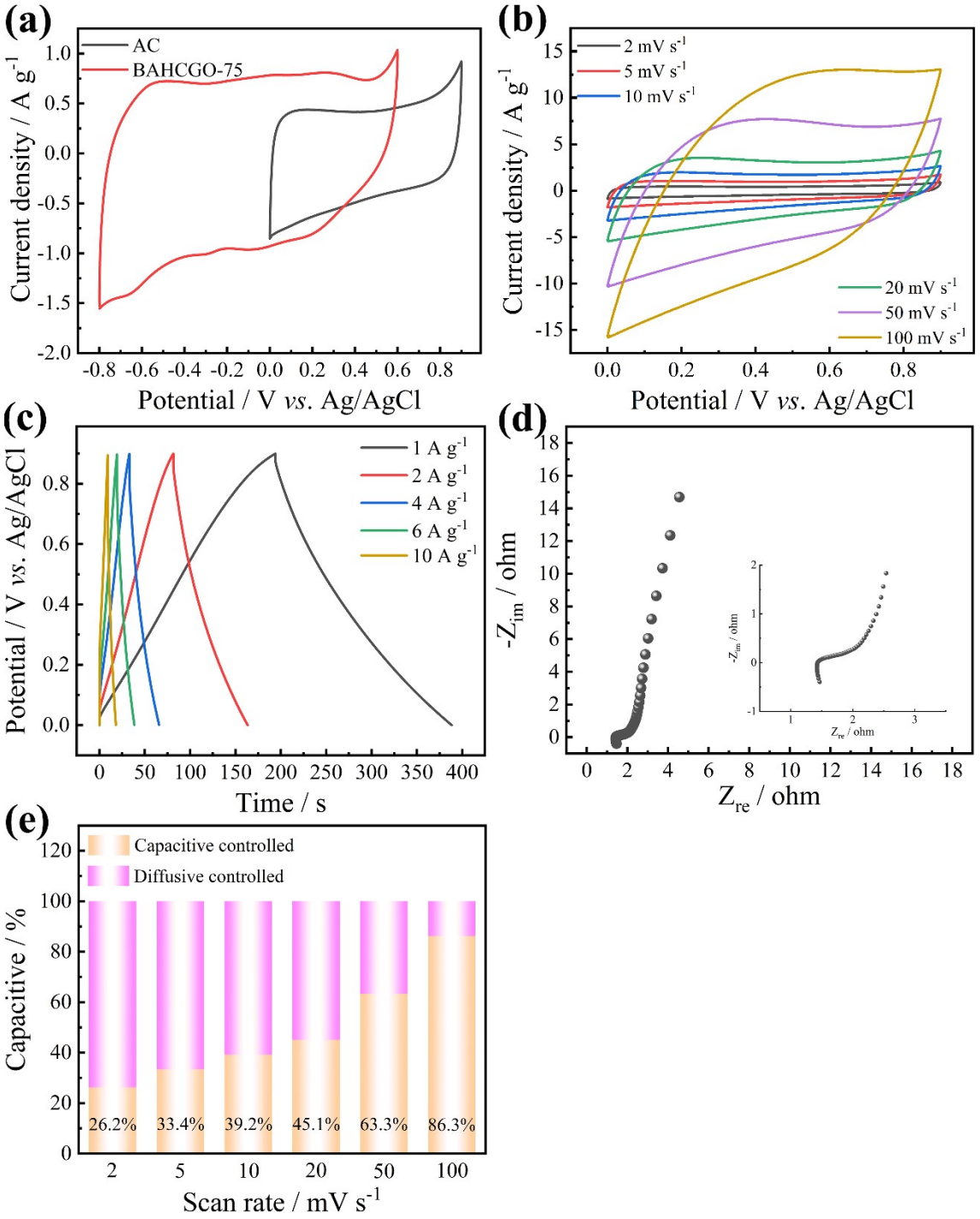

Fig. S6. (a) CV curves of AC and BAHCGO-75 at a scan rate of 2 mV s^{-1}. (b) CV curves at 2-100 mV s^{-1}, (c) GCD curve at 1-10 A g^{-1}, (d) Nyquist plots (Inset shows the magnified plot in the high-frequency region), and (e) percentages of capacitive and diffusion contributions of AC.

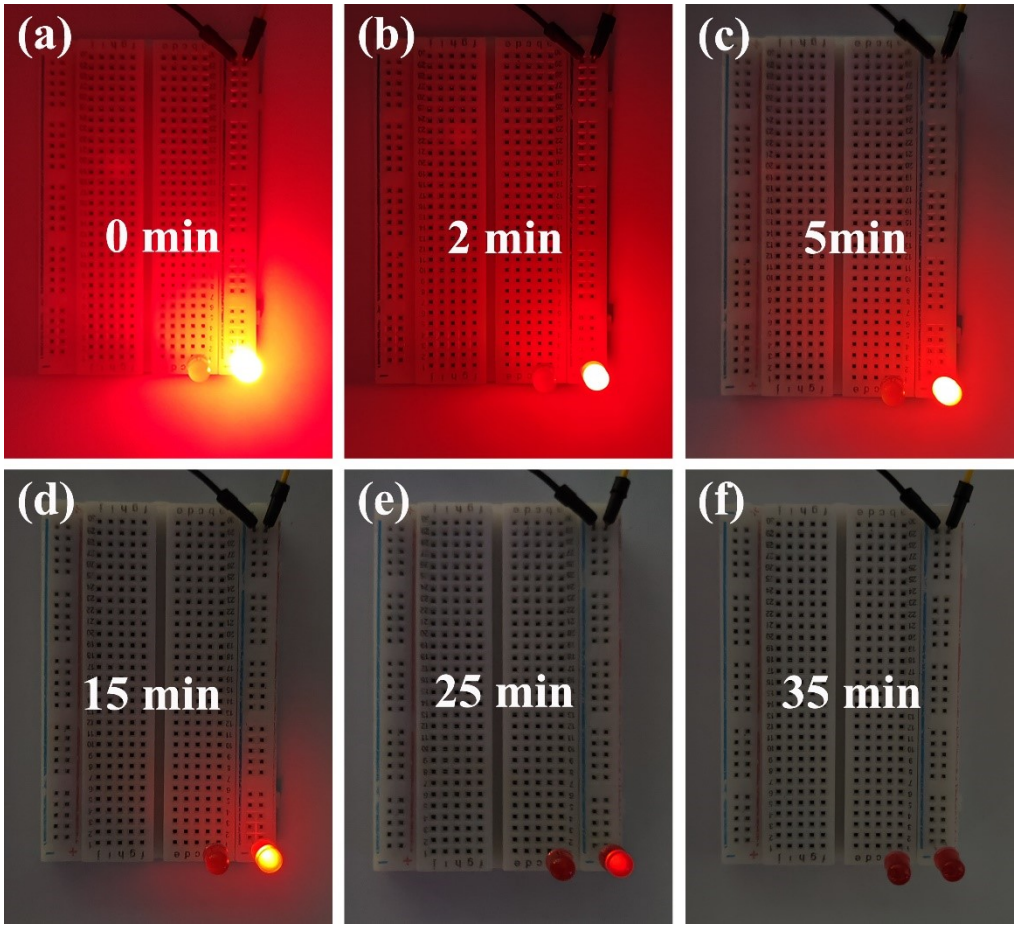

Fig. S7. Photographs presenting two BAHCGO-75//AC ASCs connected in series to successfully light up the red LDE lamp.

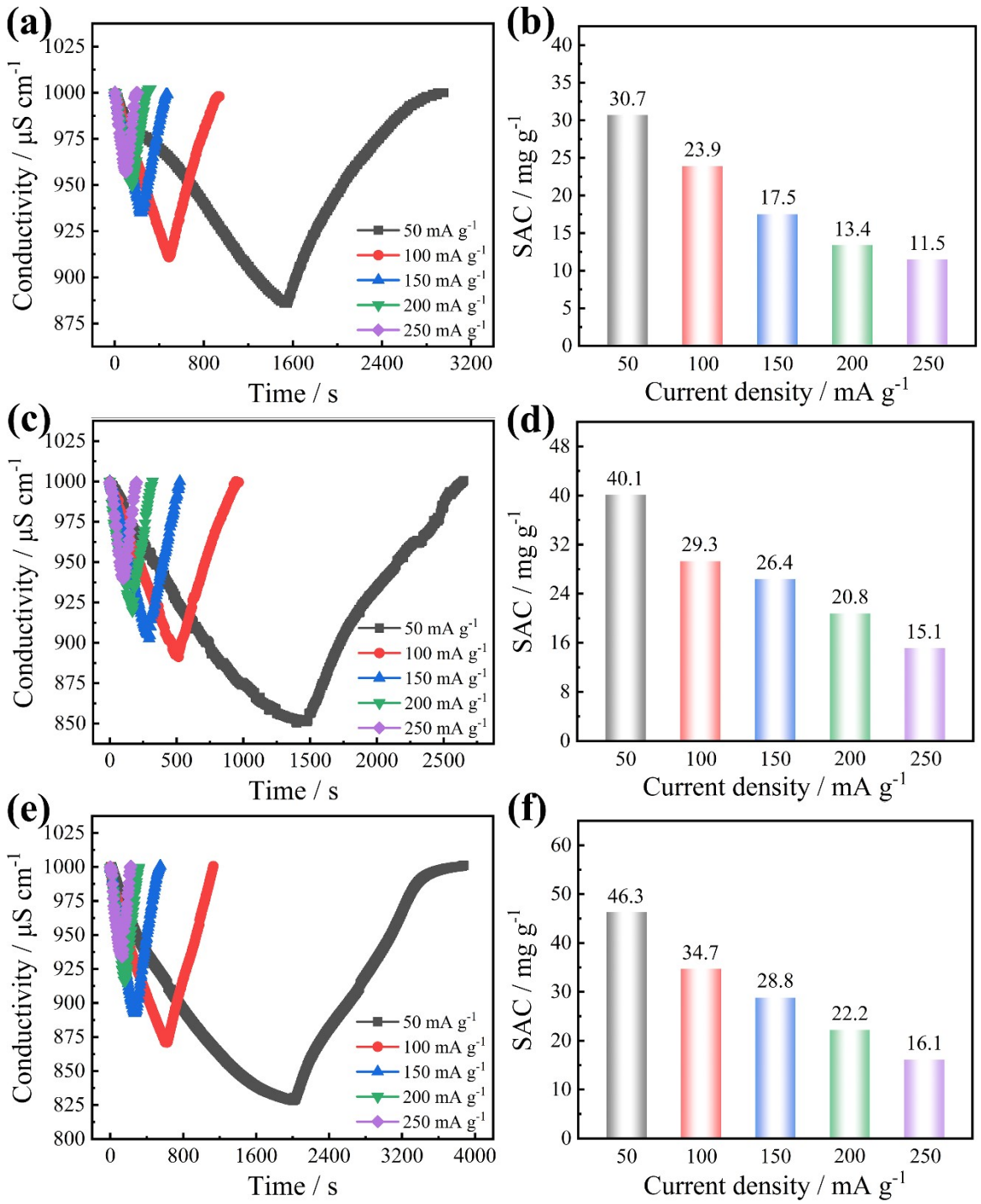

Fig. S8. Conductivity curves and SACs at different current densities of (a, b) BAHC, (c, d) BAHCGO-50, and (e, f) BAHCGO-100.

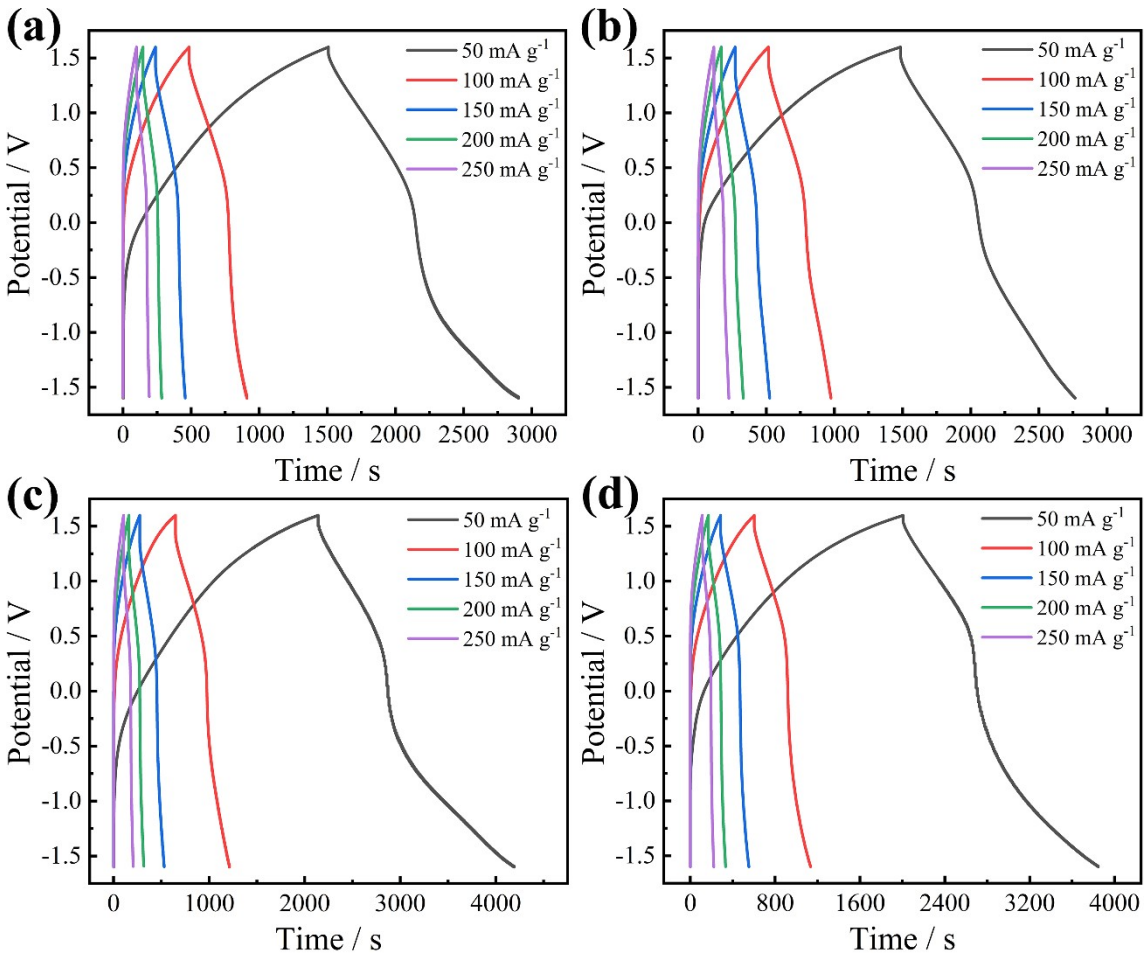

Fig. S9. Voltage response curves of (a) BAHC, (b) BAHCGO-50, (c) BAHCGO-75, and (d) BAHCGO-100 HCDI at various current densities.

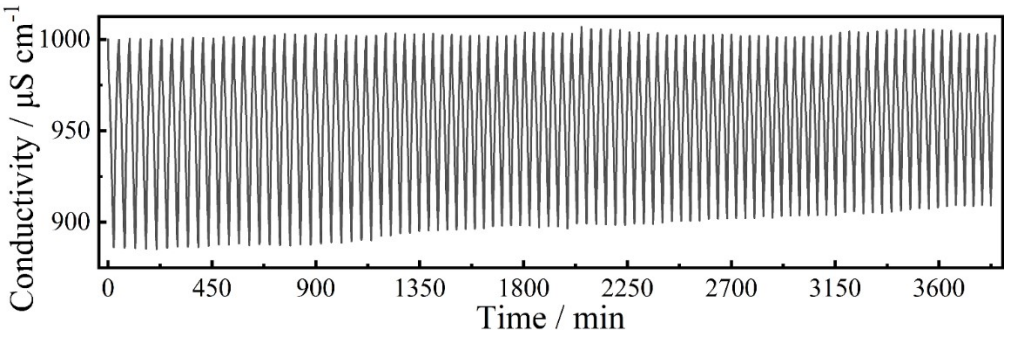

Fig. S10. Cycling performance of BAHC.

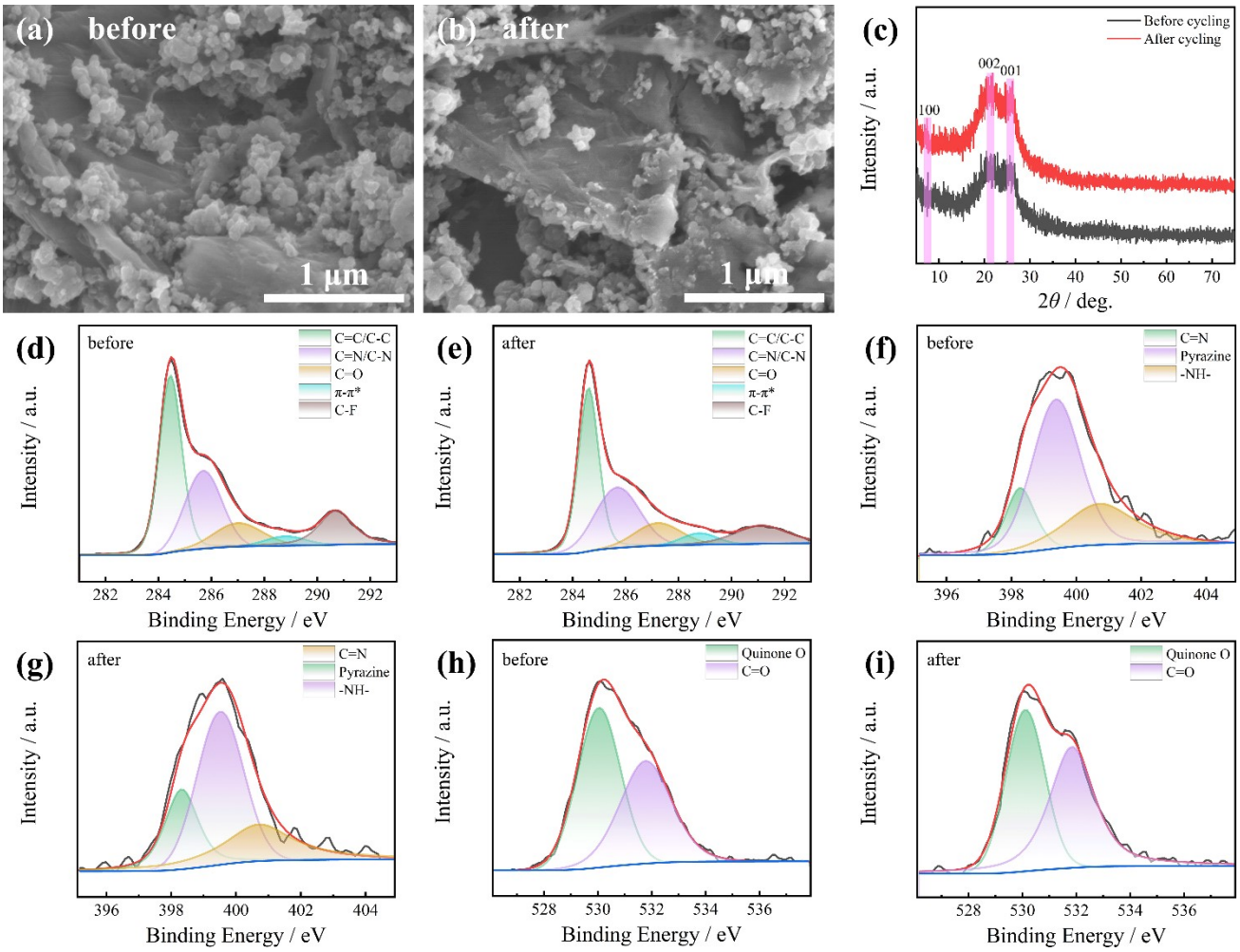

Fig. S11. (a, b) SEM images, (c) XRD patterns, and high-resolution (d, e) C1s, (f, g) N 1s, and (h, i) O 1s XPS spectra of BAHCGO-75 electrode before and after desalination/regeneration performance test.

Table S1. Comparison of desalination performances of TFPDQGO-75 with carbon-based CDI reported in the literature.

Material	SAC / mg g^{-1}	MSAR / mg g^{-1} min^{-1}	Ref.
BAHC-COF	30.7	1.68	This work
BAHCGO-75	50.5	5.40	This work
3D graphene-supported N-doped hierarchically porous carbon	25.5	0.64	[8]
Carbon foam	30.2	3.75	[9]
Heteroatom-doped hierarchical porous carbon	16.19	2.02	[10]
Defect-rich interconnected hierarchical porous carbon	31.25	3.95	[11]
KC-pre-intercalated carbon nanosheets	40.72	2.04	[12]
3D-printed thick carbon electrodes	10.67	0.28	[13]
N-doped polyporphyrin derived porous carbons	35.7	4.67	[14]
AC	8.1	0.49	[14]
N-doped hierarchically porous carbon	19.61	2.38	[15]
Zeolitic-imidazolate framework (ZIF)-derived carbon	14.19	3.99	[6]
Mg-MOF-74 derived carbon	16.82	2.28	[17]

References

1. Y.L Shao, M.F. El-Kady, J.Y. Sun, Y.G. Li, Q.H. Zhang, M.F. Zhu, H.Z. Wang, B. Dunn, R.B. Kaner, *Chem. Rev.*, 2018, **118**, 9233-9280.

2. L.M. Xu, W.Q. Zhou, S.X. Chao, Y.M. Liang, X.Q. Zhao, C.C. Liu, J.K. Xu, *Adv. Energy Mater.*, 2022, **12**, 2200101.

3. F. Y. Meng, X. B. Tu, Y. Liu, K. Wang, X. T. Xu, X. J. Li, Z. W. Gong, T. Lu, L. K. Pan, *Sep. Purif. Technol.*, 2024, **329**, 125155.

4. L.M. Xu, Y. Liu, Z.B. Ding, X.T. Xu, X.J. Liu, Z.W. Gong, J.B. Li, T. Lu, L.K. Pan, *Small*, 2023, 2307843.

5. H.B. Li, T. Lu, L.K. Pan, Y.P. Zhang, Z. Sun, *J. Mater. Chem.* **2009**, *19*, 6773-6779.

6. X. B. Tu, Y. Liu, K. Wang, Z. B. Ding, X. T. Xu, T. Lu, L. K. Pan, *J. Colloid Interface Sci.*, 2023, **642**, 680-690.

7. L.M. Xu, Z.B. Ding, Y.Y. Chen, X.T. Xu, Y. Liu, J.B. Li, T. Lu, L.K. Pan, *J. Colloid Interface Sci.*, 2023, **630**, 372-381.

8. B. Feng, Z.U. Khan, W.U. Khan, *Environ. Sci.: Nano*, 2023, **10**, 1163.

9. C.P. Li, Y.Q. Wu, J.J. An, L.X. Gao, D.Q. Zhang, J. Li, Z.X. An, *Desalination*, 2023, **559**, 116656.

10. Z. Wang, M. Gao, J. Peng, L.W. Miao, W.Q. Chen, T.Q. Ao, *Int. J. Biol. Macromol.*, 2023, **241**, 124596.

11. X.Y. Gong, S.Z. Feng, L.X. Wang, D.Z. Jia, N.N. Guo, M.J. Xu, L.L. Ai, Q.T. Ma, Q. Zhang, Z.Y. Wang, *Desalination*, 2023, **564**, 116766.

12. Q. Liu, C.Y. Zhao, M.H. Yuan, L.P. Liu, X.H. Liu, Y.J. Liu, Z.Q. Liu, L. Tong, A.G. Ying, *Desalination*, 2022, **535**, 115842.

13. M.X. Shi, K.R. Lu, H.J. Jia, X.Y. Hong, Y.H. Yan, H. Qiang, F.Y. Wang, M.Z. Xia, *Sci. Total Environ.*, 2023, **904**, 167339.

14. W. Zhang, C. Jin, Z.Y. Shi, L. Zhu, L. Chen, Y.L. Liu, H. Zhang, *Chemosphere*, 2022, **291**, 133113.

15. S.J. Wang, D.Z. Chen, Z.X. Zhang, Y. Hu, H.Y. Quan, *Sep. Purif. Technol.*, 2022, **290**, 120912.

16. H. Wang, L. Edano, L. Valentino, Y.J. Lin, V.M. Palakkal, D.L. Hu, B.H. Chen, D.J. Liu, *Nano Energy*, 2020, **77**, 105304.

17. C.P. Li, Y.Q. Wu, F.Y. Zhang, L.X. Gao, D.Q. Zhang, Z.X. An, *Sep. Purif. Technol.*, 2021, **277**, 119618.